The Impact of Parameterized Lateral Mixing on the Antarctic Circumpolar Current in a Coupled Climate Model

SARAH RAGEN

School of Oceanography, University of Washington, Seattle, Washington

MARIE-AUDE PRADAL AND ANAND GNANADESIKAN

Department of Earth and Planetary Sciences, The Johns Hopkins University, Baltimore, Maryland

(Manuscript received 17 October 2019, in final form 17 January 2020)

ABSTRACT

This study examines the impact of changing the lateral diffusion coefficient A_{Redi} on the transport of the Antarctic Circumpolar Current (ACC). The lateral diffusion coefficient A_{Redi} is poorly constrained, with values ranging across an order of magnitude in climate models. The ACC is difficult to accurately simulate, and there is a large spread in eastward transport in the Southern Ocean (SO) in these models. This paper examines how much of that spread can be attributed to different eddy parameterization coefficients. A coarse-resolution, fully coupled model suite was run with $A_{\text{Redi}} = 400$, 800, 1200, and 2400 $\text{m}^2\,\text{s}^{-1}$. Additionally, two simulations were run with two-dimensional representations of the mixing coefficient based on satellite altimetry. Relative to the 400 $\text{m}^2\,\text{s}^{-1}$ case, the 2400 $\text{m}^2\,\text{s}^{-1}$ case exhibits 1) an 11% decrease in average wind stress from 50° to 65°S, 2) a 20% decrease in zonally averaged eastward transport in the SO, and 3) a 14% weaker transport through the Drake Passage. The decrease in transport is well explained by changes in the thermal current shear, largely due to increases in ocean density occurring on the northern side of the ACC. In intermediate waters these increases are associated with changes in the formation of intermediate waters in the North Pacific. We hypothesize that the deep increases are associated with changes in the wind stress curl allowing Antarctic Bottom Water to escape and flow northward.

1. Introduction

Processes in the Southern Ocean (SO) play a significant role in the global meridional overturning circulation and the stratification of the global ocean (Naveira Garabato et al. 2016; Karsten and Marshall 2002; Gnanadesikan and Hallberg 2000). These processes are strongly influenced by the only ocean current that completely encircles the globe. The Antarctic Circumpolar Current (ACC) flows around Antarctica from west to east, tracing a roughly 25 000-km path around the world (Rintoul 2009). In terms of volume transport, the ACC is the largest ocean current on Earth, with observational estimates at Drake Passage ranging from 134 Sv (1 Sv $\equiv 10^6\,\text{m}^3\,\text{s}^{-1}$) (Whitworth and Peterson 1985; Cunningham et al. 2003) to 173.3 ± 10.7 Sv (Donohue et al. 2016). Moreover, as the only current that circumnavigates the Earth unimpeded by land, the ACC is unique in its role as a mechanism for mixing water masses that originate in different ocean basins (Worthington 1981) and is a vital component of the global general ocean circulation.

Due to the sheer volume of water transported by the ACC and its proximity to sea ice and Antarctic ice sheets, its dynamics are particularly important for climate. The ACC's large capacity for heat uptake and its influence on the meridional overturning circulation make it an important driver for salinity, heat, and carbon redistribution in the global ocean system (Giglio and Johnson 2016; Frölicher et al. 2015). The observed and projected regional trends in Antarctic ice sheet melting are likely due to oceanic forcing and advection of heat (Alley et al. 2015) associated with changes in the circulation of the ACC. Changes in temperature and salinity of SO water masses could have large repercussions for ocean circulation, sea level rise, and global climate (Alley et al. 2005; Pritchard et al. 2012). In addition to its role in the melting of sea ice and ice sheets, the SO is an important sink for anthropogenic carbon (Caldeira and Duffy 2000; Frölicher et al. 2015). The SO takes up over

Corresponding author: Sarah Ragen, sragen@uw.edu

DOI: 10.1175/JPO-D-19-0249.1

one-quarter of anthropogenic carbon each year, slowing the rate of global warming. This relatively high uptake of CO_2 does not correspond with higher levels of carbon storage, as the carbon taken up in the Southern Ocean is exported northward isopycnally to other reservoirs (Caldeira and Duffy 2000; Ito et al. 2010; Gnanadesikan et al. 2015b).

Multiple physical processes, both global and specific to the SO, influence the transport of the ACC. The westerly winds over the SO impart momentum to the ACC, which flows unimpeded by topography at shallow depths. In the zonal mean, this momentum is balanced by form drag at depth (Gille 1997; Hallberg and Gnanadesikan 2001). This implies that the northward Ekman flux at the surface must be balanced by a southward geostrophic flux of waters below the depth of topographic features in the SO. A number of authors have used this momentum balance to predict a barotropic ACC in which the transport scales as the wind stress (Munk and Palmén 1951; Wang 1994). However, the ACC is far from barotropic. As the Ekman flow is lighter than the deep inflow, the resulting circulation is associated with a tilting of isopycnals that slope down away from the continent, resulting in a thermal current shear across the current.

There are several physical regimes in which the northward Ekman and southward deep flows balance (Hallberg and Gnanadesikan 2001), resulting in different relationships between the thermal current shear in the current and the large-scale overturning. The first regime involves connecting the deep and shallow flows through surface buoyancy transformation. Southward flowing water upwells in the Southern Ocean, is initially lightened via freshening, warms as it moves northward and then is injected into the thermocline as mode and intermediate water (Gnanadesikan 1999; Gnanadesikan and Hallberg 2000). The thermal current shear is then determined both by the density contrast across the current $\Delta\rho$ (Fučkar and Vallis 2007) and by the relationship between the pycnocline and Northern Hemisphere overturning—if, as in Gnanadesikan (1999), the overturning in the north depends on $\Delta\rho$ and the square of the pycnocline depth D, for fixed $\Delta\rho$, $D \propto \sqrt{\tau}$, and the ACC transport scales as wind stress τ.

It is quite clear, however, that the Northern Hemisphere overturning is smaller than the Ekman flux in the Southern Ocean, and that not all of the upwelling water is drawn from deeper levels. There are two possible mechanisms by which this can occur. The first is the formation of stationary eddies, whereby dense water is mounded up over ridges as the ACC deflects northward over topographic features (which can be seen in hydrography in many parts of the ocean). This can result in a potentially significant fraction of the southward flow returning as northward flow over these ridges (Hallberg and Gnanadesikan 2001).

A second way of limiting the amount of deep upwelling is the presence of transient eddies. In a flat-bottomed channel, the overturning produced by a zonal wind stress steepens tilting isopycnals and increases thermal current shear up to the point where the flow becomes baroclinically unstable (Johnson and Bryden 1989; Straub 1993). Beyond this point, eddies generate an advective overturning that acts to strongly restore the flow to a level of marginal instability, largely balancing any changes in the wind-driven overturning. In such a regime, the transport is constrained below some maximum value. Such ''eddy saturation'' has been found in idealized eddy-permitting models with topography that do not include buoyancy forcing (Tansley and Marshall 2001; Munday et al. 2013) and is approximately found in realistic eddy-permitting models of the Circumpolar Current that are run out for relatively short periods of time (Hallberg and Gnanadesikan 2006).

However, as noted by Jones et al. (2011), the time scale for the low-latitude pycnocline to adjust to any imbalance between the Ekman-driven overturning and the eddy flux that compensates it (i.e., to changes in the so-called ''residual flow'') can be many hundreds of years. Thus, the degree to which the actual ACC is in a saturation regime may be overestimated. Hallberg and Gnanadesikan (2001) presented an idealized model that included each of the aforementioned three methods of closing the Southern Ocean Ekman flux and found three stable regimes: a buoyancy forcing dominated regime, an ''eddy compensation'' regime in which eddies compensate a relatively constant fraction of the overturning, and an eddy saturation regime in which increases in Ekman flux are balanced by increases in the eddy overturning. In the first regime, fractional changes in the wind stress match fractional changes in the ACC transport. In the second regime, fractional changes in the wind stresses are associated with smaller fractional changes in the transport. In the third regime, the transport is insensitive to wind stress but the eddy energy increases with wind stress (Meredith and Hogg 2006). Hallberg and Gnanadesikan (2001) argued that the real world falls in the second regime and a number of model studies since then have been consistent with this prediction (Dufour et al. 2012; Morrison and Hogg 2013; Langlais et al. 2015; Doddridge et al. 2019).

In most coupled climate models, mesoscale eddies cannot be directly simulated as they occur at spatial scales smaller than the model grids. To account for the impact of these eddies, climate models employ two eddy parameterization schemes, referred to as the Redi scheme

and the Gent–McWilliams (GM) scheme. Both are schematically illustrated in Fig. 1. The GM scheme (Fig. 1, left) represents the eddy compensation using a diffusion coefficient A_{GM} (Gent and McWilliams 1990). Horizontal fluxes then take the form $F_C = -A_{\mathrm{GM}}(\partial S/\partial z)C$, where S is the slope of the isopycnal and C is the concentration of the tracer being transported.

The Redi parameterization (Fig. 1, right) refers to mixing along neutral surfaces with diffusion coefficient A_{Redi} (Redi 1982) and fluxes given by $F_C = -A_{\mathrm{Redi}}\nabla_h C$, where $\nabla_h C$ represents the lateral tracer gradient. The actual value of A_{Redi} in the Southern Ocean is uncertain. Many studies and papers prescribe identical values for A_{Redi} and A_{GM} (Griffies 1998; Gnanadesikan et al. 2006). However, this strategy necessitates using relatively small mixing coefficients since GM coefficients greater than $1000\,\mathrm{m^2\,s^{-1}}$ damp the overturning circulation (Gnanadesikan 1999). Spatiotemporally constant values of A_{Redi} used in CMIP5 models range from 500 (Johns et al. 2006) to $2000\,\mathrm{m^2\,s^{-1}}$ (Fogli et al. 2009). Other models use spatially varying A_{Redi} ranging from values of around $200\,\mathrm{m^2\,s^{-1}}$ in gyres and 650–$1500\,\mathrm{m^2\,s^{-1}}$ in boundary currents (Gnanadesikan et al. 2006; Dunne et al. 2012; Bentsen et al. 2013). However, observational estimates of A_{Redi} ranging from 1000 to more than $10\,000\,\mathrm{m^2\,s^{-1}}$ have been obtained using floats and tracers (Ledwell et al. 1998; Gnanadesikan et al. 2013; Lumpkin and Flament 2001) whereas estimates from satellite altimetry range from less than 200 to more than $10\,000\,\mathrm{m^2\,s^{-1}}$ (Abernathey and Marshall 2013).

The transport of the ACC is often poorly simulated in climate models (Russell et al. 2006; Beadling et al. 2019). Values in the CMIP3 archive for the transport at Drake Passage range from 50 to 300 Sv with a mean transport of 144.6 ± 74.1 Sv. CMIP5 gives a slightly better range, putting transport at Drake Passage in a range from 88 to 246 Sv with a mean transport of 155 ± 51 Sv (Meijers et al. 2012; Meijers 2014; Beadling et al. 2019).

The reasons for these differences remain obscure. Beadling et al. (2019) shows that the maximum wind stress by itself explains relatively little intermodel variability, while the density gradient across the ACC explains much of it. However, so many things change between models (ocean mixing, cloud parameterizations, atmosphere gravity wave drag, atmospheric and oceanic resolution, sea ice models) that it is difficult to isolate which processes have the most important role. Certain models still use fixed global values for A_{GM} and A_{Redi}, though A_{GM} should vary temporally, horizontally, and with depth (Danabasoglu and Marshall 2007; Gent and Danabasoglu 2011) and A_{Redi} probably should too. To date, only a few studies have isolated the impact of changing eddy parameterization. Gent et al. (2001) presented a study in which winds and the mixing coefficients $A_{\mathrm{GM}} = A_{\mathrm{Redi}}$ were both varied in a coupled model. They found that increasing the mixing coefficients together decreased the strength of the current. This is expected as the eddy overturning associated with the GM coefficient scales as $A_{\mathrm{GM}}S$, and thus with a larger coefficient, a smaller isopycnal slope S would be required for the eddy flux to balance the Ekman flux, implying a lower thermal current shear. For a fixed A_{GM} coefficient, however, the overturning and ACC transport were found to increase with the wind stress. Similarly, Farneti and Gent (2011) found that the details of the GM parameterization, in particular the value at which A_{GM} is limited so as to avoid singularity in mixed layers, can also affect the ability of the eddy advection to realistically compensate changes in the Ekman flux.

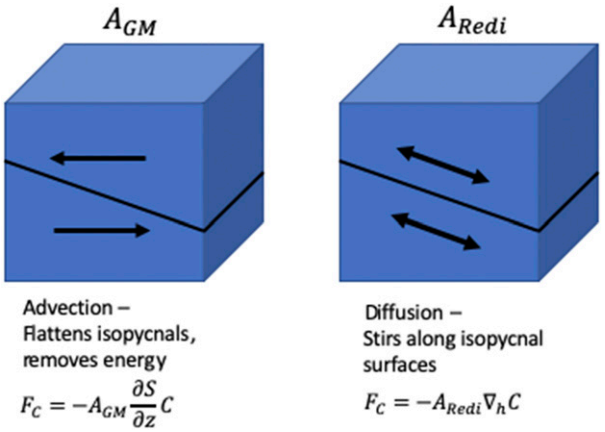

FIG. 1. Schematic of eddy impacts in the ocean. Shown are impact of (left) Gent–McWillliams parameterization and (right) Redi along-isopycnal mixing that is the focus of this manuscript.

Insofar as A_{Redi} primarily mixes along isopycnals, warming or cooling along isopycnals should be balanced by salinification or freshening. It might therefore be assumed that changing A_{Redi} would not significantly alter isopycnal slopes and thus would have a relatively limited impact on the ACC, so that one could attribute the sensitivity seen by Gent et al. (2001) entirely to the A_{GM} coefficient. However, as we will demonstrate in this paper, when A_{Redi} is allowed to vary independently of A_{GM} over a range comparable to that seen within the CMIP5 ensemble within a single coupled climate model it can have a significant impact on the ACC. This is both because such changes in A_{Redi} produce changes in SSTs (Pradal and Gnanadesikan 2014) which in turn impact the winds over the SO, as well as because they produce changes in high-latitude stratification and convection. In the following section of this paper, we will introduce the model used and the experimental design.

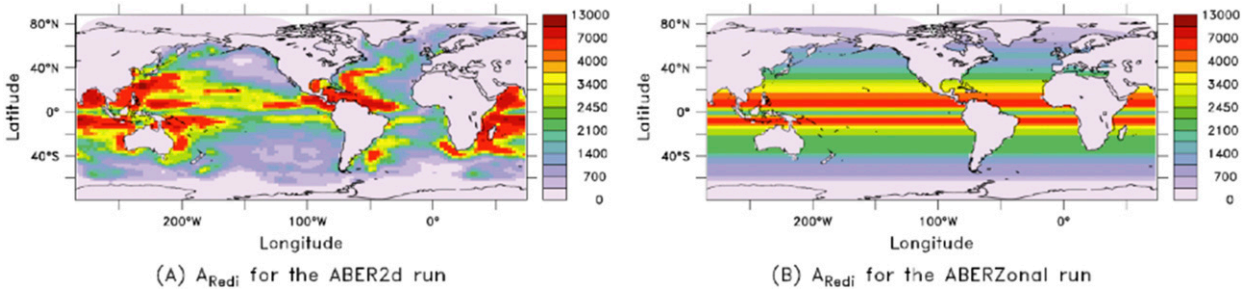

FIG. 2. Mixing coefficients from Abernathey and Marshall (2013) altimetric product ($m\,s^{-2}$) mapped to the model grid. (a) Full 2D field, used in the ABER2D simulation. (b) Zonally averaged version used in the ABERZONAL simulation.

Section 3 presents the results of six different simulations with different representations of A_{Redi}, allowing us to evaluate how much of the range seen in CMIP5 could be attributed to variations in this parameterization. In the last section of the paper, we will discuss what our results imply about the dynamics of the Circumpolar Current.

2. Model description

For this study, the physical model used is the Geophysical Fluid Dynamics Laboratory (GFDL) fully coupled Coupled Model 2 with Modular Ocean, coarse grid (CM2Mc). The model includes separate atmosphere, ocean, sea ice, and land components that are linked through a flux coupler. The atmosphere model grid consists of 24 vertical levels, with a 3.75° longitudinal resolution and a 3° latitudinal resolution. The ocean model has 28 vertical levels and a nominal 3° × 1.5° resolution, with a latitudinal resolution that is finer in the equatorial waveguide and in Drake Passage latitudes. The model contains up-to-date representations of many processes, including atmospheric convection, oceanic vertical mixing, and eddy mixing. Climatological annual cycles of ozone and 12 classes of aerosols (black carbon, sulfate, organic carbon, sea salt, and eight size classes of dust) are prescribed. Additionally, global mean atmospheric concentrations of three greenhouse gases (CO_2, CH_4, and N_2O) are fixed throughout the run.

Four simulations were conducted with the diffusive eddy mixing coefficient A_{Redi} set to spatiotemporally constant values of 400, 800, 1200, and 2400 $m^2\,s^{-1}$. These runs are referred to as AREDI400, AREDI800, AREDI1200, and AREDI2400, respectively. Additionally, two simulations were made in which the A_{Redi} was estimated using a field of surface velocities estimated from satellite altimetry (Abernathey and Marshall 2013). The resulting field of A_{Redi} is shown in Fig. 2a and shows relatively small values in the Southern Ocean but much higher values in the subtropical gyres. A simulation made with this field is referred to as ABER2D. To evaluate whether changes due to employing this 2D field were due to the full 2D structure of the field or merely to the latitudinal variation in the field, an additional simulation was made with a zonally averaged version of Fig. 2a, shown in Fig. 2b and referred to as ABERZONAL. We note that the fields are both isotropic and independent of depth, conditions that are unlikely to hold in the real world. However, there is no consensus in the literature for how diffusion coefficients should fall off with depth and previous work (Gnanadesikan et al. 2015a) suggests relatively high coefficients in the deep southeast Pacific. Our results should thus be taken as exploring possible sensitivities rather than as the final word on the impact of lateral mixing. The impact of changing A_{Redi} on hydrographic properties is reported in Pradal and Gnanadesikan (2014), Gnanadesikan et al. (2015a,b), and Bahl et al. (2019).

Modern values of oceanic temperature and salinity are used to initialize the simulations. A simulation with greenhouse gases and aerosols held at 1860 values was spun up for 1500 years with $A_{\mathrm{Redi}} = 800\,m^2\,s^{-1}$. After 1500 years, five simulations are branched off this trunk run with different mixing coefficients. All six simulations are then run for 1000 years. In each of the five branches, the majority of the surface temperature change occurred in the first 50 years. The last century, years 900–1000, was used to establish the climate in each case. The differences between the centennially averaged ACC transports across the different runs are larger than the ±2-Sv range in centennially smoothed transport within the control simulation. However, it is by no means clear that the final state associated with equilibration of the deep ocean has been reached. The results should thus be taken as indicative of the variance in ACC that can be induced by uncertainty about what value of A_{Redi} to prescribe.

The parameterization of advective subgrid-scale mesoscale eddy transport is represented using a spatially varying coefficient A_{GM} with a minimum coefficient of

$200\,m^2\,s^{-1}$, and a maximum of $1400\,m^2\,s^{-1}$. A_{GM} is computed from the local vertical shear of the horizontal velocity and width of the baroclinic zone (Gnanadesikan et al. 2006) following earlier work by Griffies (1998). Insofar as A_{Redi} causes changes in the stratification it also induces variation of the value of A_{GM}. As in Galbraith et al. (2011) the effective maximum slope used to compute the overturning streamfunction S_{max} is 0.01.

The model used in this study is similar to the GFDL 1° coupled model (CM2.1) but with a coarser resolution so as to decrease the computational cost of spinning up long-term simulation suites. Despite the coarser resolution, CM2Mc features updates over CM2.1 including improvements to subgrid-scale mixing parameterizations in the ocean (Galbraith et al. 2011) and a higher value of S_{max}. There are physics in the ACC that are not included in this model, but as this paper explores eddy parameterizations in climate models, the coarse resolution of CM2Mc suits the purposes of this study. Higher-resolution models can resolve eddies and might show less of an impact on eastward transport due to eddy saturation effects. The sensitivity of this coarse-resolution model to variations in parameters is not necessarily directly comparable to a model of finer resolution. While our results might differ from higher-resolution models and the real ocean, the phenomena in CM2Mc are consistent with other climate models, such as those included in CMIP5.

3. Results

Transport through the Drake Passage in this study's model simulations is consistent with observations and CMIP5 models. AREDI400, AREDI800, and ABER2D, with respective Drake Passage transports of 169.7, 161.0, and 158.5 Sv, fall within 2σ of the observational estimate of 173.3 ± 10.7 Sv (Donohue et al. 2016). This criterion is employed by Beadling et al. (2019) to assess the accuracy of ACC transport in CMIP5 models. The AREDI1200, AREDI2400, and ABERZONAL runs all lay just below the observational range of uncertainty by 6 Sv or less (Table 1). Furthermore, the zonal mean wind stress produced by the models in this study compare well with the ERA-Interim atmospheric reanalysis (Dee et al. 2011), the NCEP reanalysis (Kistler et al. 2001), and the range of CMIP5 models (Beadling et al. 2019).

To understand the differences between mixing cases, we first examine the changes in surface wind stress, temperature, and salinity that arise from altering the A_{Redi} coefficient. Figure 3 shows a contour map of differences in surface properties between AREDI2400 and AREDI400. Surface wind stress (Fig. 3a) shows both a weakening over latitudes of 45°–65°S and a strengthening over latitudes of 30°–45°S. This is a signature of both a weakening in the peak winds and a small equatorward shift. Maximum decreases in surface wind stress reach $0.02\,N\,m^{-2}$, which amounts to a 10% change with respect to the peak values (Seviour et al. 2017) between the low and the high mixing cases. Sea surface temperature (Fig. 3b) increases with A_{Redi} over almost the entire ocean (with exceptions in few small regions, off the east coast of New Zealand, in the South Atlantic around 40°S, and off the coast of South Africa). The greatest temperature difference is an increase of about 4°C west of Drake Passage and just off the ice shelf. As this warming reduces the equator-to-pole temperature gradient, it is broadly consistent with the warming driving the change in wind stress, though the stress changes are considerably more zonal in character. Increasing lateral eddy mixing generally increases salinity, but causes a small decrease in a region within the Ross Sea (Fig. 3c). The increase in salinity and temperature as mixing increases can be understood in terms of additional transport of salt along isopycnals destabilizing the wintertime thermocline and allowing more upward mixing of heat in polar regions (Pradal and Gnanadesikan 2014).

Figure 4a shows the barotropic quasi-streamfunction for the low mixing case (AREDI400) relative to the southern tip of South America (so that the value at the tip of the Antarctic peninsula represents the transport through Drake Passage). Note that the term quasi-streamfunction accounts for the fact that surface freshwater fluxes that cause a relatively small amount of divergence, which is ignored to compute the streamfunction. The other plots in Fig. 4 show the differences between the streamfunction in other mixing cases and the low mixing case (colors) with contours of the streamfunction in the low mixing case overlaid (contours).

TABLE 1. Averaged diagnostics across the model suite. The second column shows eastward transport in Drake Passage (Sv). The third column shows the averaged eastward transport in the latitude band from 40° to 65°S (where as seen in Fig. 6 the zonal mean velocities are eastward). Column 4 shows the mean wind stress from 45° to 65°S, covering the region where changes are generally in the same sense.

Model	Drake Passage transport (Sv)	65°–40°S transport (Sv)	Mean wind stress (Pa)
AREDI400	169.7	193.5	0.103
AREDI800	161.0	179.1	0.098
AREDI1200	146.6	157.3	0.092
AREDI2400	145.8	155.8	0.091
ABER2D	158.5	167.9	0.096
ABERZONAL	148.6	159.2	0.093

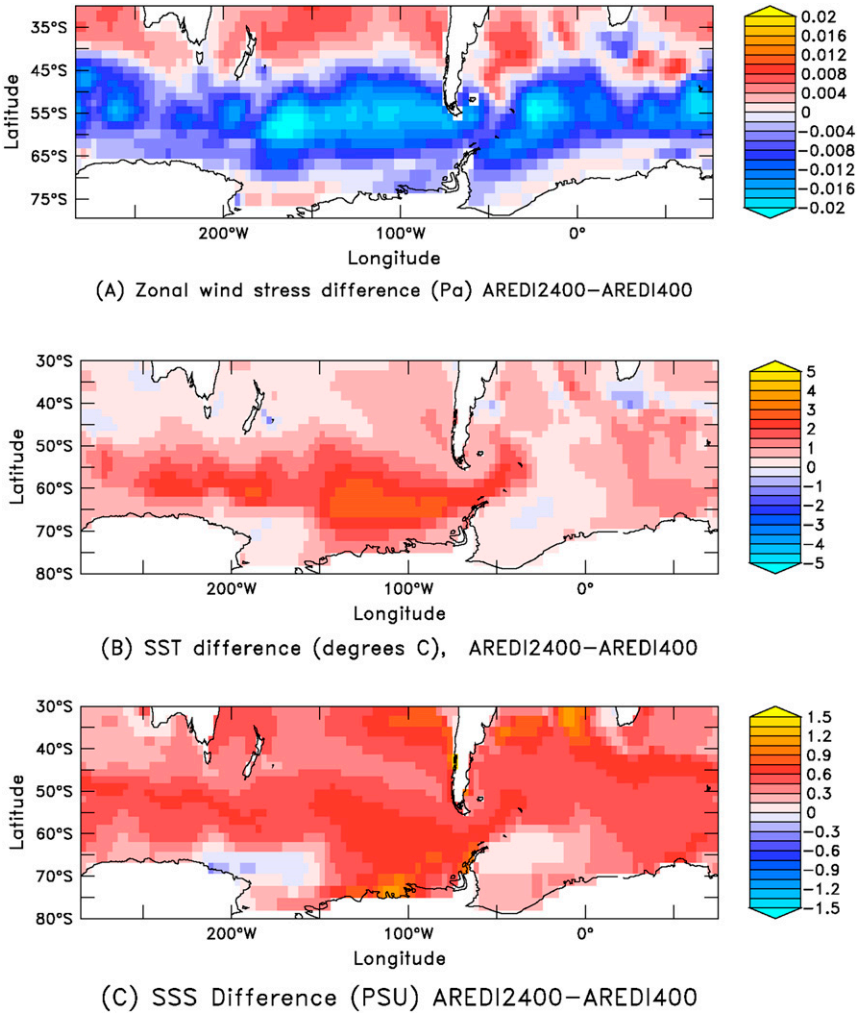

FIG. 3. Differences between high mixing (AREDI2400) and low mixing (AREDI400) cases. (a) Zonal wind stress at the air–sea interface (N m^{-2}). (b) Sea surface temperature (°C). (c) Sea surface salinity (psu).

In general, higher mixing coefficients produce lower transports in Drake Passage and in the zonal mean, though the differences between AREDI2400 and AREDI1200 are relatively small. As shown in Table 1, increasing A_{Redi} from 400 to 2400 reduces the transport in Drake Passage by 24 Sv (about 14%) and reduces the average eastward transport across all longitudes by 37 Sv (about 20%). The altimetry-based estimates of mixing produce results that lie between the AREDI400 and AREDI2400 cases. Note that the ABER2D simulation shows much larger changes in ACC transports than does the ABERZONAL case, with a drop that is almost twice as large at Drake Passage. This suggests that the full 2D structure of the mixing in ABER2D plays an important role in determining the response of the Southern Ocean, possibly because high mixing coefficients are displaced away from frontal zones.

In all cases, the transport anomaly relative to AREDI400 is negative south of 55°S, indicating reduced eastward circulation. This suggests that increasing A_{Redi} corresponds to a slowdown in the component of the eastward flow associated with the subpolar gyre. Moreover, in some places, like the central South Pacific and east of the Drake Passage, the negative transport anomaly extends northward to about 50°S. The transport anomaly relative to AREDI400 is positive north of 55°S, suggesting a shift between transport being carried in the ACC and in the subtropical gyres. Figure 4 shows a slowdown of the subtropical gyre in the southern Pacific, and a northward shift in the eastward transport in the Atlantic and Indian basins. In each mixing case, the largest decreases in eastward transport in the Southern Ocean occur before the current enters the Drake Passage at about 120°W, where the Ross Sea gyre also decreases in

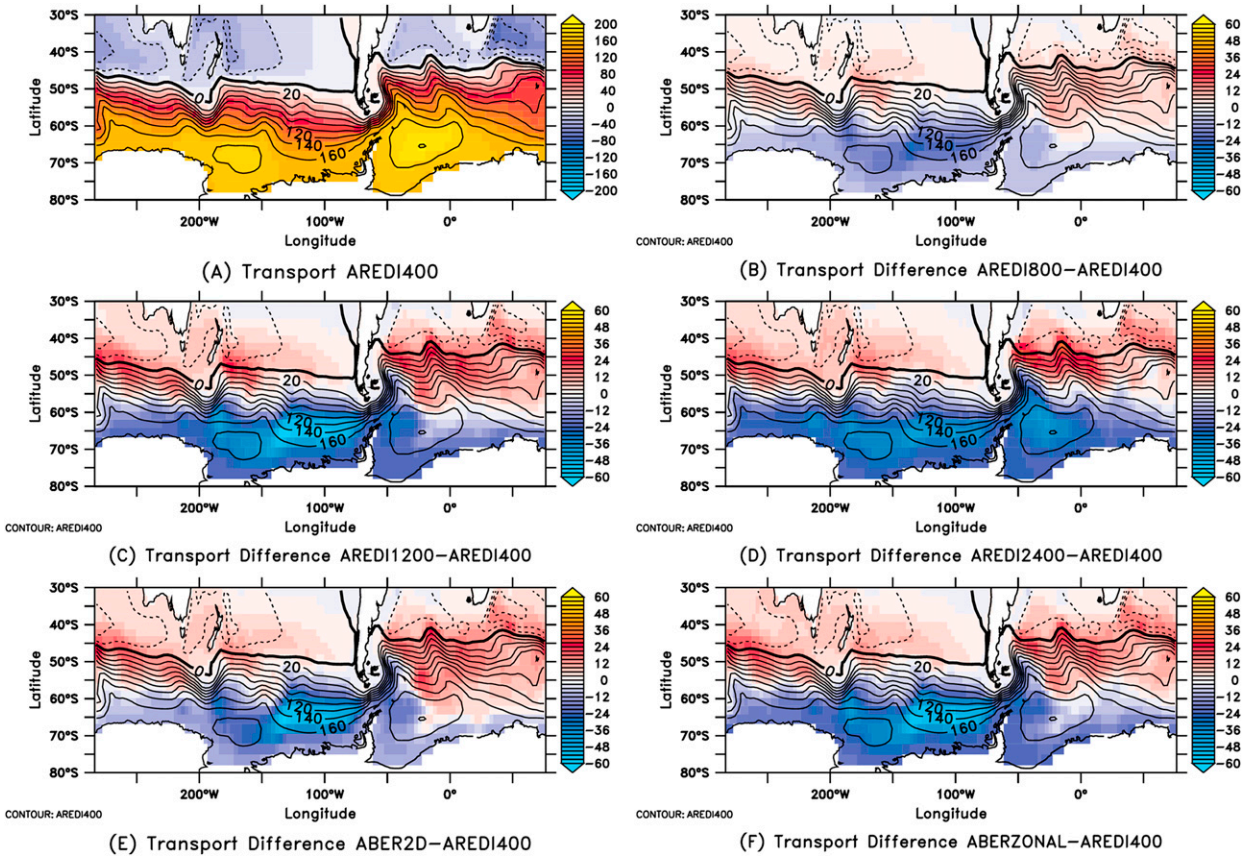

FIG. 4. Plots showing the streamfunction computed using zonal transport and differences relative to the lowest constant mixing case anomalies (Sv). Colors show (a) AREDI400 transport; (b) transport difference, AREDI800 − AREDI400; (c) transport difference, AREDI1200 − AREDI400; (d) transport difference, AREDI2400 − AREDI400; (e) transport difference, ABER2D − AREDI400; and (f) transport difference, ABERZONAL − AREDI400. Contours always represent the AREDI400 transport.

strength. Relative to AREDI400, AREDI800 shows a decrease of 8.7 Sv in Drake Passage, but more than 24 Sv in the central Ross Sea (and 13.5 Sv in the zonal average). The changes are generally smaller in the Drake Passage than at other locations in the Southern Ocean. This indicates that the Drake Passage is not a reliable indicator of significant changes in the averaged eastward volume transport in the Southern Ocean as whole.

a. Momentum and its balances within the Southern Ocean

Because the flow through Drake Passage may not be fully representative of the whole Southern Ocean, we instead examine the zonal means of transport and wind stress. As shown in Fig. 5, the higher the lateral mixing parameter A_{Redi}, the lower the transport and zonal wind stress. Relative to AREDI400, zonally and depth-averaged velocities (Fig. 5a) in AREDI2400 decrease by around 30% in Drake Passage latitudes and by around 20% north of that. In contrast, the wind stress (Fig. 5c) varies much less. Peak wind stress (at 51°S) drops from 0.128 to 0.114 Pa, an 11% decrease, similar to the change in average wind stress in the region where winds decrease (65°–45°S). The changes in zonal mean velocity (Fig. 5b) look similar to the changes in wind stress (Fig. 5d) with corresponding peak anomalies. However, it is noteworthy that even though eastward winds decrease throughout the Southern Ocean, the current response in the Ross Sea is in the reverse direction as the winds (which show a westward acceleration in this latitude band).

While larger drops in wind are associated with larger changes in the current, it seems clear that theories in which the ACC transport is linearly proportional to the wind stress (i.e., Wang 1994; Marshall 2003) cannot explain such a disproportionate response. Such theories fall short of describing the response of the ACC to changes in wind stress. The fractional change in transport is smaller in magnitude than the fractional change in wind due to compensation from eddies (Langlais et al. 2015).

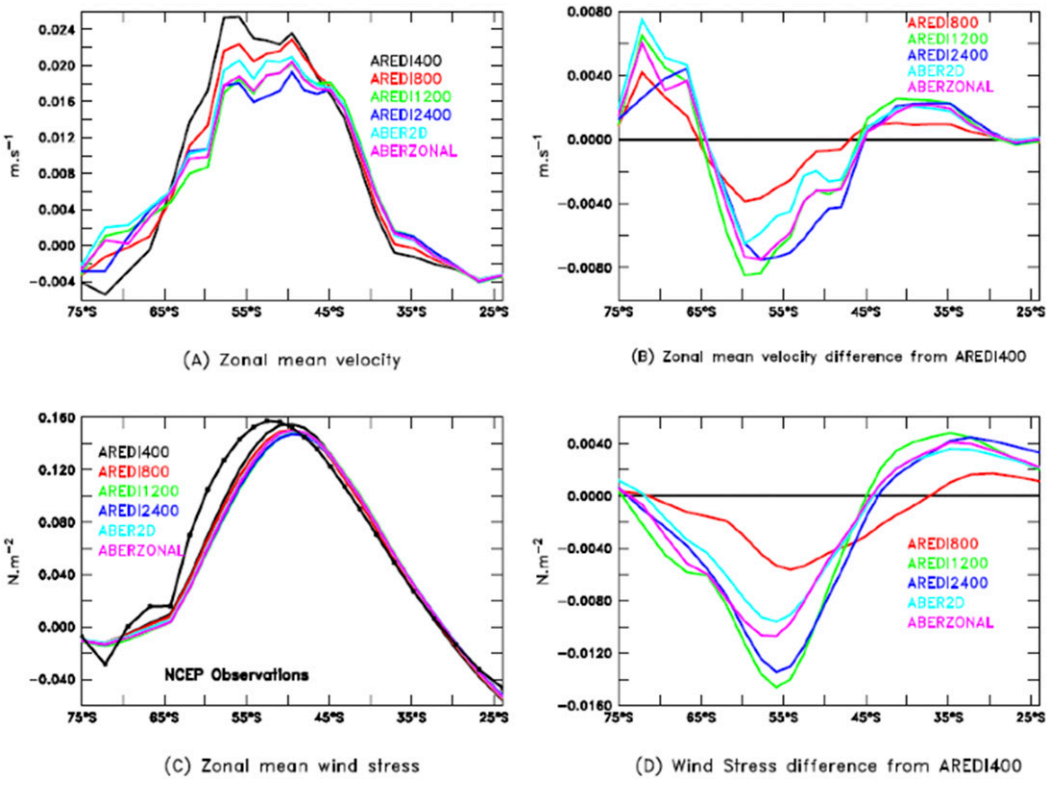

FIG. 5. Momentum in the Southern Ocean. (a) Zonal mean velocity for all six mixing cases is shown from 80° to 20°S. (b) Zonal mean velocity difference relative to AREDI400 for the other five cases. (c) Zonal mean wind stress (Pa); NCEP observations are shown by the thick black line with symbols. (d) Zonal mean zonal wind stress difference relative to AREDI400 for the other five cases.

If eddy compensation is to explain why the fractional change in transport is *greater* than the fractional change in wind, A_{GM} would have to increase with A_{Redi} (Gent et al. 2001). Instead (as shown in Fig. 6) the A_{GM} coefficients get smaller as the mixing coefficients increase, with a larger drop for AREDI1200 and AREDI2400 (Figs. 6c,d) than for AREDI800 (Fig. 6b). The maximum parameterized eddy overturning in depth space in the Southern Ocean also drops, falling from −20.5 Sv in AREDI400 to −14.7 Sv in AREDI1200. In density space, a similar drop is seen from −18.5 Sv in AREDI400 to −13.0 Sv in AREDI1200. Similar values are found for ABER2D and ABERZONAL, though surprisingly AREDI2400 has a larger eddy overturning of −18 Sv in depth space and −15.9 Sv in density space. Both the changes in A_{GM} and eddy-driven overturning are in the wrong direction to explain the modeled changes in ACC transport, as less momentum is pumped out of the surface layer into the deep layer by eddies as A_{Redi} increases.

Before further examining the impacts of the change in wind stress, we examine the mechanisms behind such changes. The black line in Fig. 7a shows the difference in surface wind stress between the AREDI2400 and AREDI400 simulations. As seen by looking at the red line in Fig. 7a, differences in the divergence of the column-integrated atmospheric poleward eddy flux of zonal momentum largely explains these differences in surface stress (especially over the Southern Ocean where topographic form stress is zero), indicating that the black line in Fig. 7a effectively shows the difference in downward flux of eastward momentum.

What accounts for the changes in eddy momentum flux? As shown in Fig. 7b, there is a basic relationship between the upper-atmosphere (200 mb; 1 mb = 1 hPa) geopotential height gradient across the Southern Ocean (40°–65°S) and the poleward eddy zonal momentum flux into the Southern Ocean (at 45°S) integrated across all pressure levels. A larger drop in geopotential and thus a stronger atmospheric jet corresponds to a greater poleward eddy zonal momentum flux at 40°S. This relationship explains both the interannual variability seen in the model and the difference between the two models. The blue and black point clouds in Fig. 7b are offset, indicating that the AREDI2400 model never experiences the strongest gradients in zonal mean

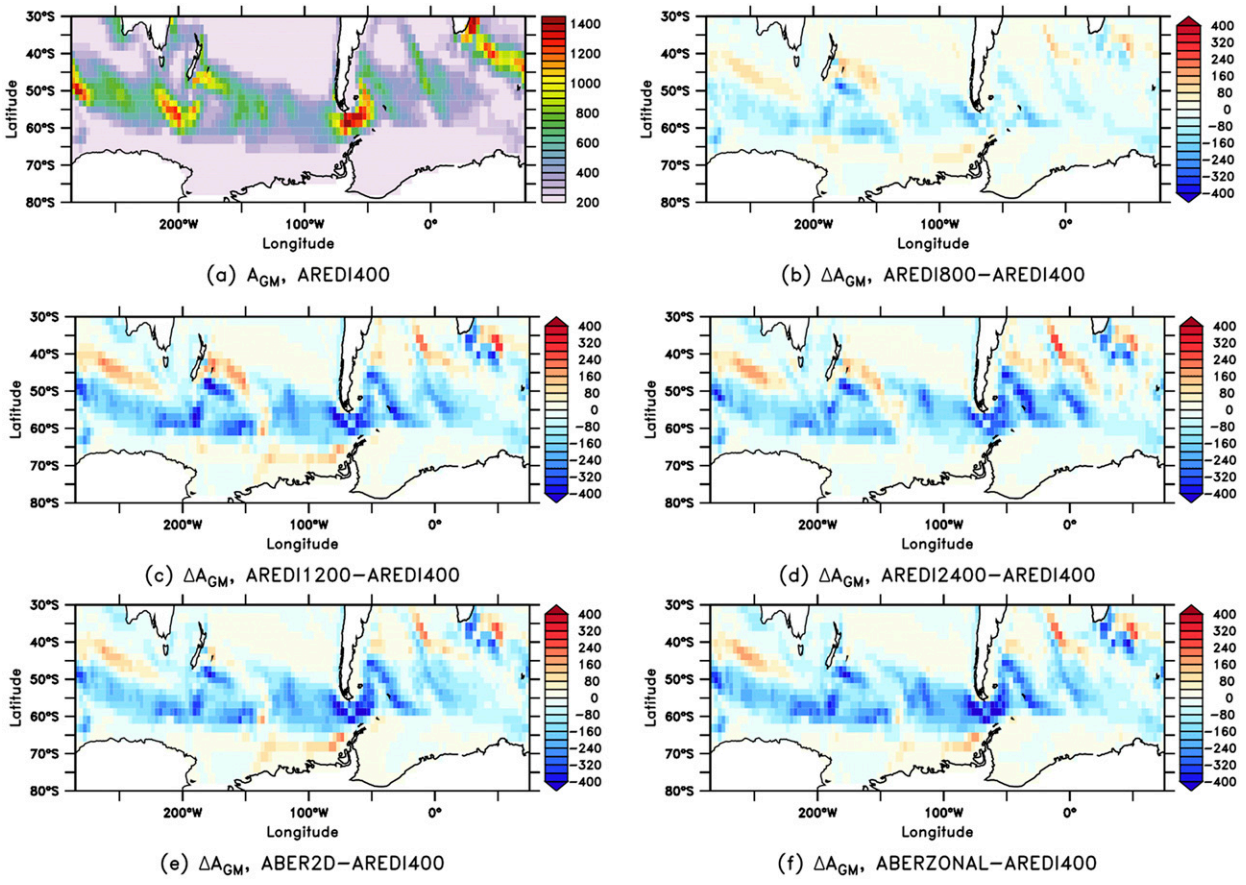

FIG. 6. GM coefficients A_{GM} ($m\,s^{-2}$) in the Southern Ocean across the model suite: (a) AREDI400 simulation, (b) difference in A_{GM} AREDI800 − AREDI400, (c) difference in A_{GM} AREDI1200 − AREDI400, (d) difference in A_{GM} AREDI2400 − AREDI400, (e) difference in A_{GM} AREDI800 − ABER2D, and (f) difference in A_{GM} AREDI800–ABERZONAL.

geopotential height seen in AREDI400, and as a result the mean geopotential height difference between 40° and 65°S is 37 m (around 5%) lower. The relationship between eddy momentum flux and geopotential height gradient in our simulations is consistent with that seen in the ERA-Interim reanalysis (the dashed line in Fig. 7b shows the mean slope and range over the period from 1979 to 2010). Our model shows more variability than the ERA-Interim reanalysis (possibly because the 200 years shown here allow for us to see the impacts of interdecadal variability which may be damped in the ERA record), but the marginal sensitivity between the overall change in upper layer winds and eddy momentum flux is consistent.

The difference in 200-mb geopotential height ϕ_{200} between the AREDI2400 and AREDI400 simulation (Fig. 7c) is dominated by a rise over Antarctica. Warmer atmospheric temperatures at pressures greater than 200 mb drive the increase in ϕ_{200} over the globe. The increase in ϕ_{200} is smallest at latitudes around 40°S, where atmospheric temperatures change very little between AREDI2400 and AREDI400. Poleward of this latitude, changes in the temperature of up to 2°C are seen when averaged over the entire troposphere. Such changes are quite sufficient to produce the tens of meters of change in ϕ_{200}. Higher temperatures over Antarctica act to decrease the geopotential height gradient. This causes a smaller amount of momentum convergence into the region of maximum wind speed and results in lower wind stress at the sea surface (Starr 1948).

b. *Thermal current shear and buoyancy*

As noted above, the impact of winds on ACC transport can be indirect, as the winds affect water mass transformation and change the density contrast across the ACC, in turn altering the thermal current shear. We computed the differences in eastward thermal current shear from the differences in the density field at each longitude and integrate it vertically to get current

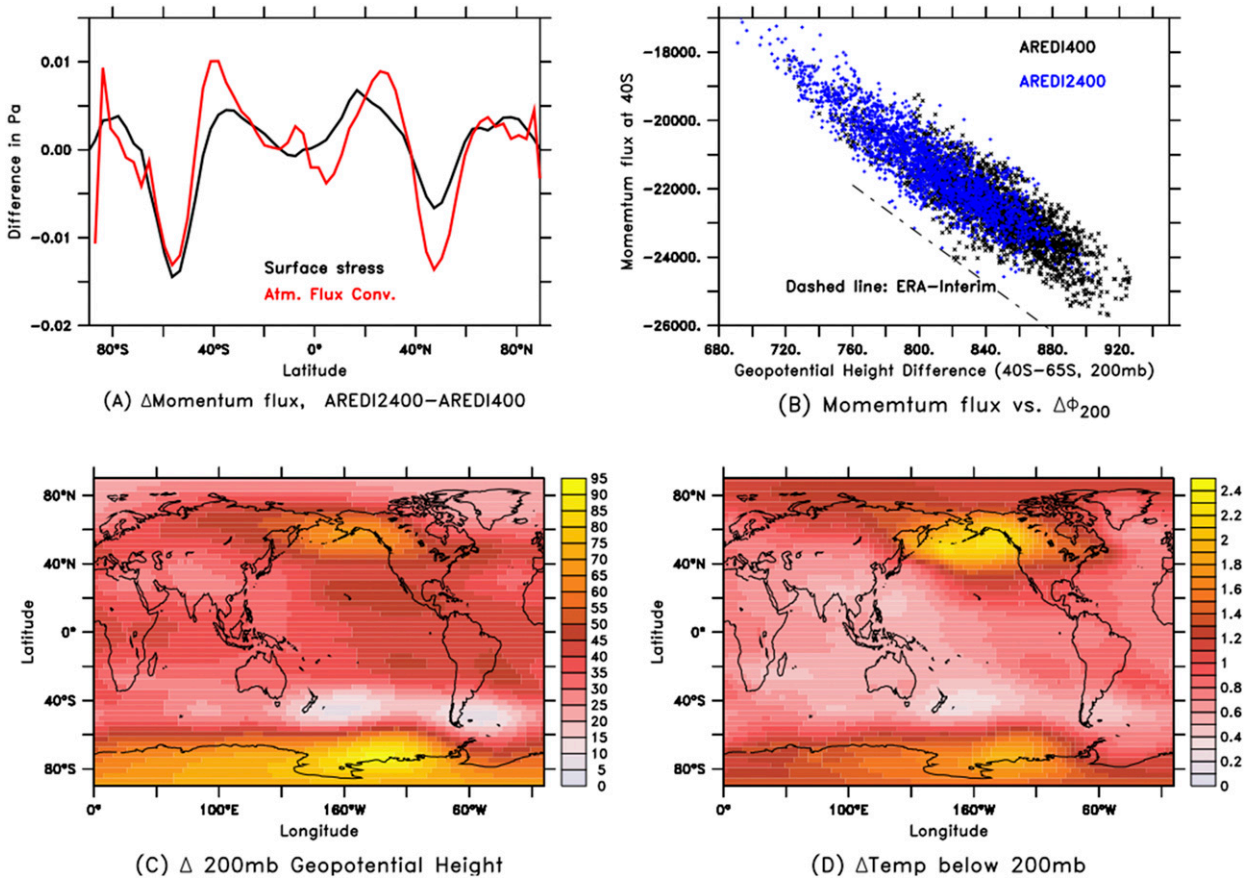

FIG. 7. Dynamically relevant changes in the atmosphere between AREDI2400 and AREDI400. (a) Changes in momentum transport. The black line shows the change in surface wind stress. The red line shows the change in momentum flux convergence. (b) Relationship between momentum flux at 40°S and geopotential height difference between 40° and 65°S. Symbols show AREDI400 (black) and AREDI2400 (blue). The dashed line shows equivalent range and slope of relationship in the ERA-Interim reanalysis. (c) Change in 200-mb geopotential height, illustrating an increase over Antarctica (m). (d) Change in temperature at heights below (pressures above) 200 mb, illustrating the connection between an increase in geopotential height and surface warming (°C).

velocity relative to a depth of 4500 m. As shown in Fig. 8, the resulting prediction of the velocity change across the ACC between AREDI2400 and AREDI400 (Fig. 8b) looks similar to the actual change (Fig. 8a). Similar results have been found for other pairwise comparisons between our simulations but are not shown here. This suggests [consistent with the recent results of Beadling et al. (2019)] that we should focus on the density changes across Drake Passage rather than on bottom pressure gradients and barotropic transport as the primary explanation for the differences in ACC transport across the model suite.

Cross sections of the differences in potential temperature, salinity, and in situ potential density between AREDI2400 and AREDI400 are shown in Fig. 9. The left-hand column shows values north of the ACC channel at 40°S and the right-hand column shows values south of the channel at 65°S. North of the channel, there is a temperature increase at the surface above about 500 m of depth of about 1°C. Below that, the temperature decreases with maximum temperature decrease of about 2°C with increasing A_{Redi}. The change in salinity is similar, with a 0.5-psu increase at the surface above depths of around 1500 m. Below that, the salinity decreases by about 0.3 psu. This results in an increase in density throughout the entire depth of the cross section of about 0.2 kg m^{-3}.

On the southern side of the channel, a similar pattern emerges with temperature and salinity increases at the surface and decreases at depth. The temperature increases by about 1°C at the surface, but this increase is confined to the top 200 m except in a small region at about 150°E where it dips down to about 500 m. The salinity increases by about 0.2 psu above 500 m except

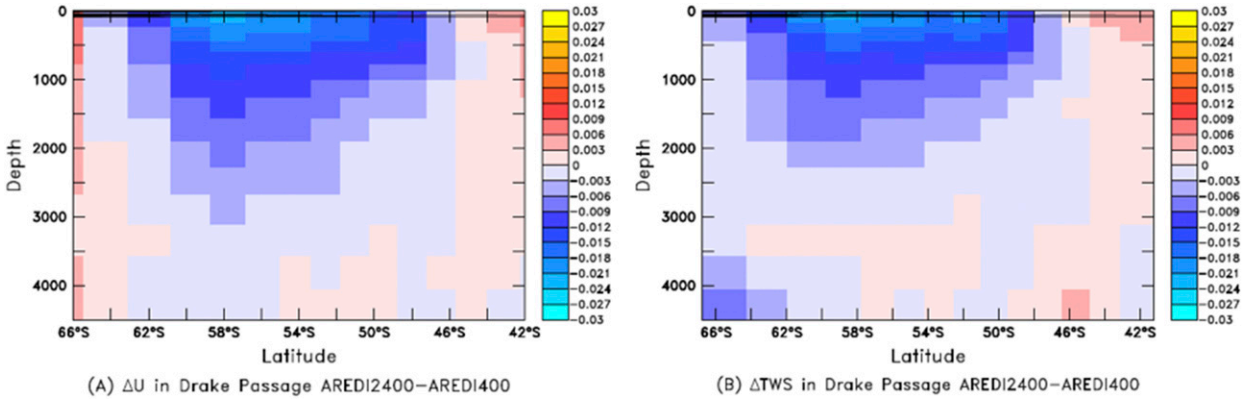

FIG. 8. Comparison of changes between the AREDI2400 and AREDI400 case. (a) Zonal mean velocity ($m\,s^{-1}$). (b) Velocity change relative to 4500 m computed from thermal current shear ($m\,s^{-1}$).

for in the same region where the depth of the isohaline surface dips to 1500 m. Here, on the southern side of the channel, the change in density is much smaller than on the northern edge of the channel. Nowhere on the southern edge of the channel does the density increase by more than $0.2\,kg\,m^{-3}$.

While altering the mixing changes the mean density throughout the ocean, such changes are only marginally relevant for the thermal current shear. To better focus on the relevant density changes we now look at zonal mean density anomalies relative to the zonally averaged value at the same depth at 65°S, defining

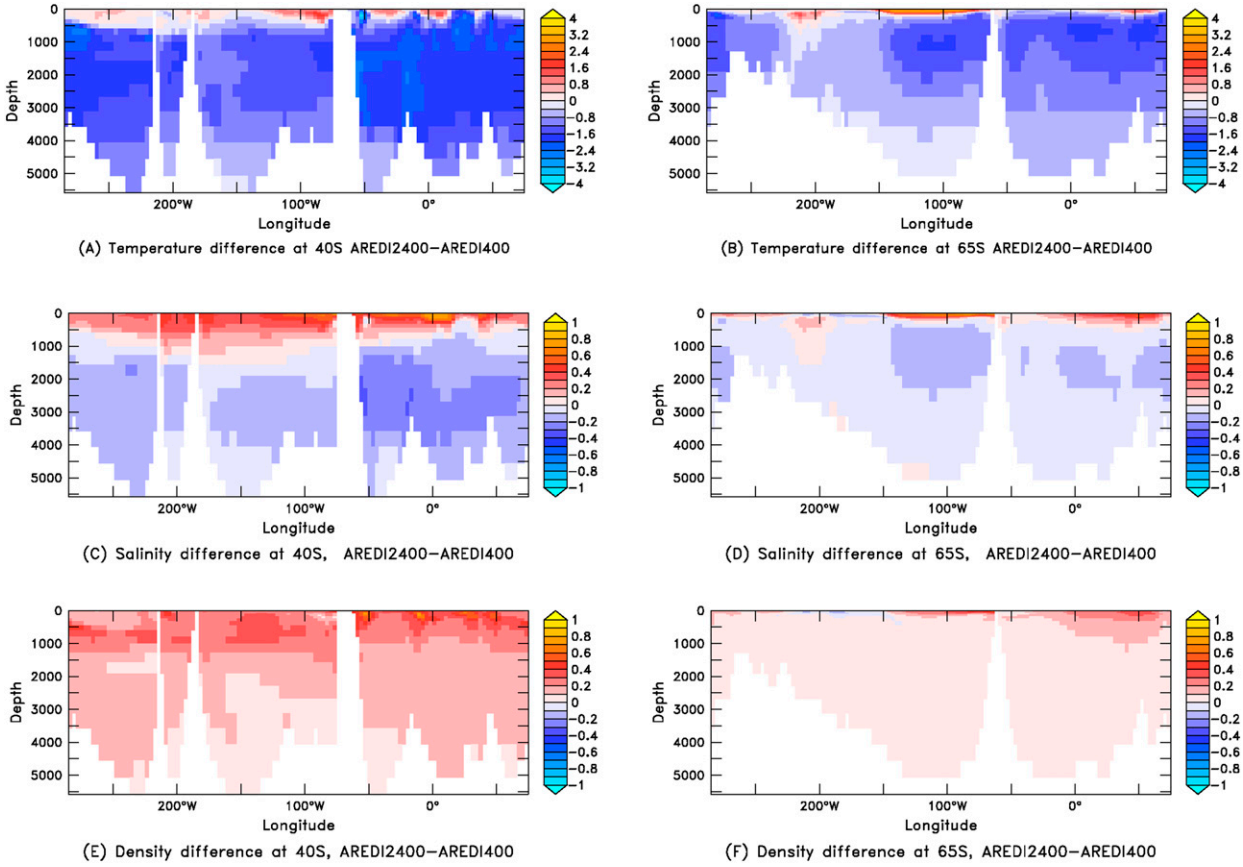

FIG. 9. Circumpolar cross sections of changes between AREDI2400 and AREDI400 in (a),(b) potential temperature (°C), (c),(d) salinity (psu), and (e),(f) in situ density ($kg\,m^{-3}$). Shown are changes at (left) 40°S and (right) 65°S.

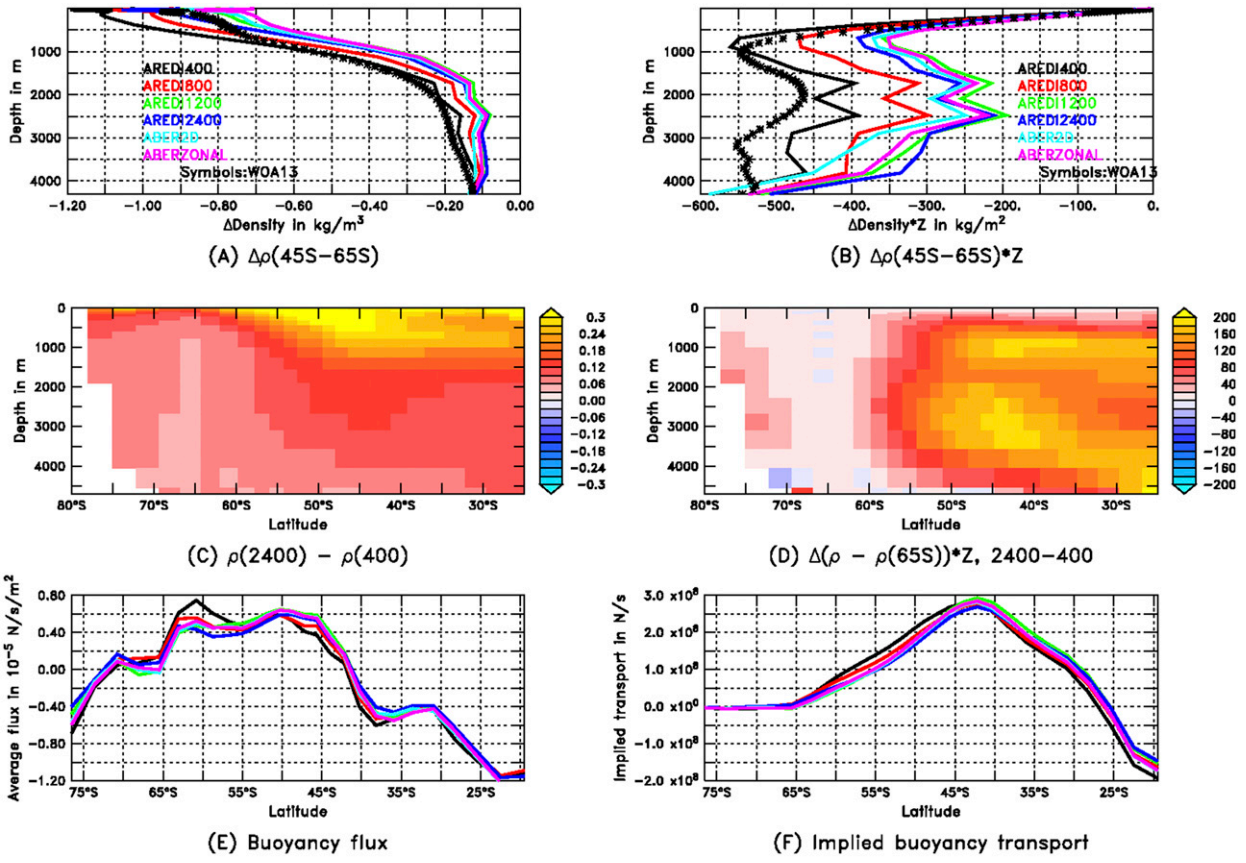

FIG. 10. (a) Profiles of zonally averaged difference in density between 45° and 65°S for each simulation and observations. (b) Profiles of zonally averaged difference in density between 45° and 65°S multiplied by depth, highlighting locations most important for changing the baroclinic transport. (c) Zonally averaged change in density relative to 65°S between AREDI2400 and AREDI400. (d) Zonally averaged change in density relative to 65°S multiplied by depth. (e) Zonally averaged surface buoyancy flux. (f) Cumulatively integrated buoyancy flux, indicating transport that would be required to balance the fluxes in (e).

$$\Delta\overline{\rho_{65S}} = [\overline{\rho(z,\phi,\text{Model})} - \overline{\rho(z,\phi=65\text{S},\text{Model})}] - [\overline{\rho(z,\phi,\text{AREDI400})} - \overline{\rho(z,\phi=65\text{S},\text{AREDI400})}], \quad (1)$$

where $\rho(z,\phi,\text{Model})$ is the density at a certain depth and latitude in the specific A_{Redi} model run, $\rho(z,\ \phi\ =\ 65\text{S},$ Model) is the density at the same depth, at latitude 65°S, and in the same model run, $\rho(z,\ \phi,$ AREDI400) is the density at the same depth and latitude in AREDI400, and $\rho(z,\ \phi\ =\ 65\text{S},$ AREDI400) is the density at the same depth at latitude 65°S in AREDI400. This enables us to better compare density changes between simulations on a single plot without having to visually correct for different offsets in density.

Profiles of $\Delta\overline{\rho_{65S}}$ for each model simulation and observations are shown in Fig. 10a. The AREDI400 case is closest to observations, and the density difference across the current decreases as A_{Redi} increases. There seem to be greater changes in $\Delta\overline{\rho_{65S}}$ above 1000 m with changing A_{Redi}. The raw density differences between AREDI400 and AREDI2400 are shown in Fig. 10c. Consistent with Fig. 9c, the changes within the Southern Ocean are small. The relative densification of the mode and intermediate waters is a far larger signal. Additionally, increasing A_{Redi} results in a tongue of slightly denser water penetrating below 2000 m.

The zonal transport M_x relative to the bottom can be found by double integrating the equation for shear relative to a motionless bottom velocity with the following equation:

$$M_x = \int_{z=-D}^{0} v(z,y) \int_{y=\phi_s}^{\phi_n} dy\, dz = \int_{z=-D}^{0} \int_{z'=-D}^{z} \int_{y=\phi_s}^{\phi_n} \frac{\partial v}{\partial z} dy\, dz'\, dz, \quad (2)$$

where v is meridional velocity, z' is the vertical coordinate (positive upward), ϕ_s is the latitude on the southern side of the ACC, and ϕ_n is the latitude on the northern

side of the ACC. Note that following Beadling et al. (2019) we perform this integration relative to 4500 m. Since we integrate upward from the bottom, changes in thermal current shear at depth will have a much larger impact on the total transport than changes near the surface (as the impact of shear on transport represents a double integration). If we only consider the component of the shear that is due to thermal current, Eq. (2) becomes

$$M_x \approx \frac{g}{f(55\mathrm{S})}\int_{z=-D}^{0}\int_{z'=-D}^{z'}[\rho(45\mathrm{S},z') - \rho(65\mathrm{S},z')]\,dz'\,dz$$
$$= \frac{g}{f(55\mathrm{S})}\int_{z=-D}^{0}[\rho(45\mathrm{S},z) - \rho(65\mathrm{S},z)]z\,dz, \tag{3}$$

where g is the acceleration due to gravity, $f(55\mathrm{S})$ is the Coriolis parameter at 55°S, and ρ is density. Equation (3) shows that changes in density at depth have a greater impact on transport than changes at the surface. When we multiply the density change in Figs. 10a and 10c by the depth (allowing us to properly compare the impact of density changes on transport), we get the profiles in Fig. 10b and the section in Fig. 10d, respectively. Figure 10b shows a relatively constant impact of the cross-channel density differences below 1000 m on the thermal current shear, though there is decrease in the impact of the shear at about 2000 m Fig. 10d shows the difference between the AREDI2400 and AREDI400 models, which highlights two regions of dynamically important density change, centered at around 1000 and 3000 m, that contribute roughly equivalent increments to the total transport.

These differences are not easily explained in terms of changes in surface fluxes. The surface buoyancy flux Q_{buoy} is computed as

$$Q_{\mathrm{buoy}} = -g(\alpha Q/c_p - \beta_s F_w S), \tag{4}$$

where α is the coefficient of thermal expansion, Q is the surface heat flux, c_p is the specific heat of seawater, β_S is the haline contraction coefficient, F_w is the surface freshwater flux (kg s^{-1}), and S is the surface salinity. As shown in Fig. 10e, the changes in the surface buoyancy flux are relatively small. There is a little more buoyancy gain between 65° and 55°S and a little less loss north of these latitudes in AREDI400 as compared to the other model runs, but the other runs do not show much contrast from each other. We can integrate these fluxes with longitude and cumulatively integrate them with latitude to get the meridional buoyancy transport needed to balance them, as shown in Fig. 10f. All the models show that the Southern Ocean is a region of buoyancy gain and export to lower latitudes. However, the magnitude of buoyancy export is essentially identical across the simulations, although the latitude of the maximum shifts equatorward (along with the peak in wind stress) as A_{Redi} increases. It is not obvious how this could explain why we see larger increases in density (decrease in buoyancy) to the north of the Drake Passage latitudes than within them. This suggests that we may need to look more carefully at why water mass properties appear to shift across the models.

c. Water masses

We examine differences in water masses by looking at changes in salinity between the AREDI2400 and AREDI400 simulations in the 500–1500- and 2000–3000-m depth bands that, as seen in Fig. 10d, have a big impact on thermal current shear (Fig. 11). The intermediate waters (left column, Fig. 11) show large changes in salinity emanating from the North Pacific, which propagate into the Southern Hemisphere. There is a salinification of intermediate waters in the Pacific basin in AREDI2400 as compared to AREDI400, which can be seen in Fig. 11c. This causes densification north of the ACC at about 40°S. We interpret these changes as arising from the destratification of the North Pacific, which strengthens the circulation in the Pacific basin. Increasing mixing tends to decrease stratification in the North Pacific as surface waters increase in salinity, reducing the difference in salinity across the winter halocline (Pradal and Gnanadesikan 2014; Gnanadesikan et al. 2015a; Bahl et al. 2019). Vertical exchange in the North Pacific is strongly dependent on the magnitude of this salinity contrast (Gnanadesikan et al. 2015a; Bahl et al. 2019) and its reduction leads to increased overturning in the Pacific basin (see Fig. 10 in Bahl et al. 2019). The overturning circulation draws salty subtropical waters into the Northeast Pacific and shallows the pycnocline throughout the global ocean.

By contrast, at depth, the biggest changes in salinity are seen within the Southern Ocean. As A_{Redi} increases, temperature and salinity decrease at depth in the Southern Ocean. We quantify this by examining T–S plots between 2000 and 4000 m in these two simulations, shown in Fig. 12. Black symbols indicate the water mass properties between 60°S and the equator, while contours show the potential density referenced to 3000 m. The red stars indicate the average water mass properties at 40°S. In the AREDI400 case, the mean water mass properties at this latitude (T = 3.5°C, S = 34.83 psu) are close to the midpoint between Antarctic and North Atlantic water masses. A quantitative water

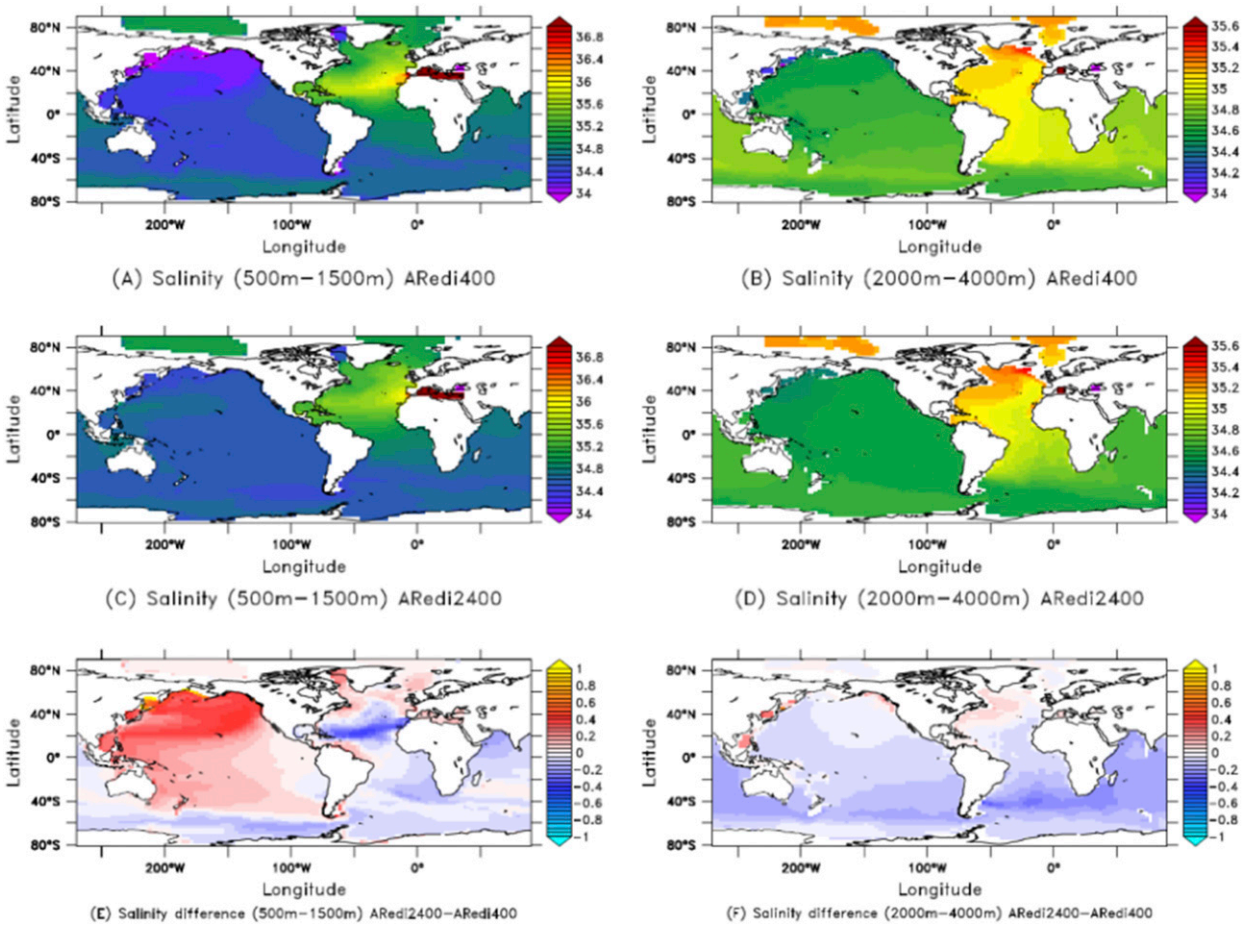

FIG. 11. Salinity fields at (left) 500–1500 and (right) 2000–4000 m. Values for (a),(b) AREDI400, (c),(d) AREDI2400, and (e),(f) the difference between the two. Note that the increase in Pacific sector salinity within the Southern Ocean shallower depths can be tracked back to the North Pacific, while the differences at greater depth are largest within the Southern Ocean.

mass analysis shows that at this latitude, 49% of the water is of North Atlantic origin ($T = 5°C$, $S = 35.12$ psu), 21% is Circumpolar Deep Water from the deep Southern Ocean ($T = 0.5°C$, $S = 34.6$ psu) and the remaining 30% is from the intermediate water classes ($T = 3°C$, $S = 34.6$ psu). In the AREDI2400 case, by contrast, the mean temperature and salinity ($T = 1.98°C$, $S = 34.66$ psu) lie much closer to the intermediate water end member ($T = 2°C$, $S = 34.53$ psu), suggesting that only 22% of the water at 40°S is of North Atlantic ($T = 4.5°C$, $S = 35.15$ psu) origin, 29% is Circumpolar Deep Water, and 49% is intermediate water. Increasing A_{Redi} leads to a decrease in North Atlantic water but an increase in Circumpolar Deep water and intermediate water. As there is no deep water formation at these latitudes, we interpret these changes as a northward shift in the front between fresher but denser Antarctic Bottom Water and saltier but lighter North Atlantic Deep water. It appears that when A_{Redi} is larger, Antarctic water more readily escapes the Southern Ocean, reducing the deep cross-ACC density gradients and thus the transport.

What accounts for the shift in the deep front? As shown in Fig. 13a, the region of increased density in AREDI2400 lies immediately below a region where the wind stress curl increases. Because the wind stress curl in this region is negative, this change makes the region less favorable to downwelling. A hypothesis, then, is that the change in wind stress curl propagates all the way to the bottom because the mean currents in this region (black line, Fig. 13b) are faster than the baroclinic Rossby wave speed $c = \beta L_R^2$ (red line, Fig. 13b). This means that the baroclinic concentration of momentum near the surface described by Gill (1982) is unable to hold. Currents which flow much faster than the baroclinic Rossby wave speed display an equivalent-barotropic structure and as such the flow at depth is closely related to the surface flow

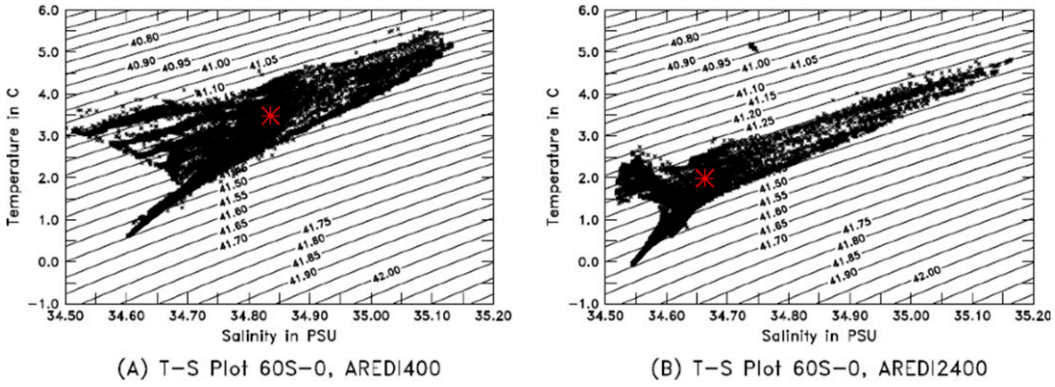

FIG. 12. *T–S* plots for the Southern Hemisphere from 60°S to the equator in the (a) AREDI400 model and (b) AREDI2400 model. Contours show potential density referenced to 3000 m. The red star shows average value at 40°S.

[see also Hughes (2005) for more discussion of this mechanism].

4. Conclusions

In this study, we observed dynamical changes that arose in the circulation in the Southern Ocean due to variations in the lateral eddy mixing. Our results demonstrate that in a coupled climate model, increasing the value of A_{Redi} acts in the same general sense as increasing the value of A_{GM}. Both parameters should be taken into account as important to the circulation in the Southern Ocean. Using a coupled model helps to illuminate the multifaceted relationships between mixing, sea surface temperatures, winds, and subsurface density structure. In contrast to model studies such as Gnanadesikan and Hallberg (2000) where surface densities were fixed to observations, coupled models allow for changes in winds, SSTs and subsurface density to be dynamically consistent.

Increasing A_{Redi} resulted in a notable slowing of the transport of the ACC. However, the greatest changes in transport occur outside of the Drake Passage, suggesting that modelers may need to consider a wider range of diagnostics than just the transport within the passage when assessing the representation of the ACC in models. The relative change in transport was about 2.5 times greater in magnitude than the relative change in wind stress, suggesting that simple models that predict that the transport is directly proportional to wind stress (Wang 1994) or wind stress curl (Warren et al. 1996) are unlikely to be correct. We hypothesize that the

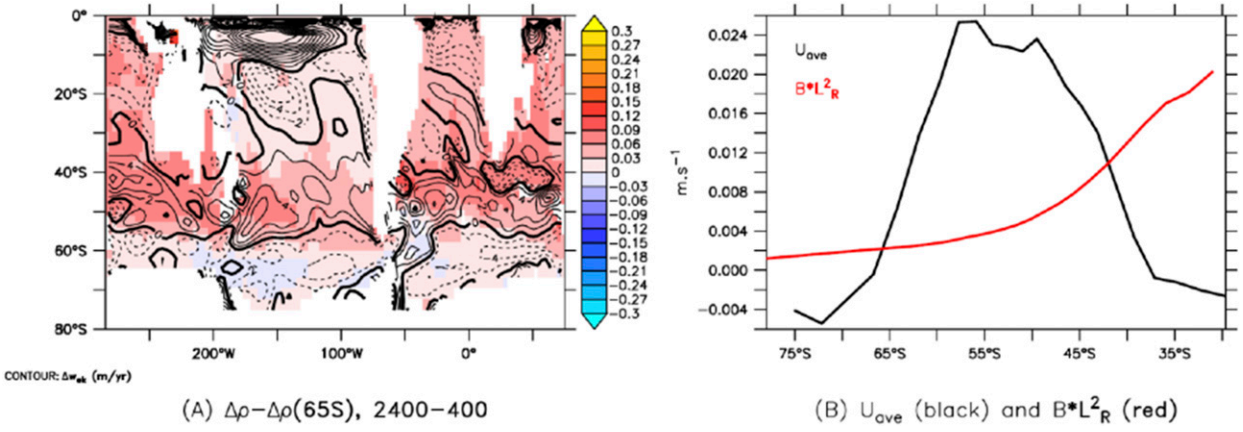

FIG. 13. Explaining deep density changes. (a) Southern Hemisphere changes in density at 400 m (colors; kg m^{-3}) overlaid with contours of wind stress curl anomalies showing that the most intense changes are found in latitudes with positive anomalous wind stress curl. (b) Comparison of zonally and depth-averaged velocities (black line) and zonally averaged Rossby wave speed (red line), showing that between about 65° and 40°S the mean velocities exceed the first baroclinic Rossby wave speed and so changes in wind stress curl would be expected to be communicated to the bottom.

changes in transport in the Southern Ocean were caused by alterations to the density structure to the north of the ACC channel, although naively we would not expect varying A_{Redi} to produce such a change, in conjunction with increased wind stress curl in the Southern Ocean. An increase in density in intermediate and deep waters on the northern edge of the ACC appears to explain the change in transport. By destratifying the North Pacific and increasing northern overturning (Gnanadesikan et al. 2015a; Bahl et al. 2019), increasing A_{Redi} shallows the pycnocline and increases the density of intermediate waters to the north of the ACC. This reduces the density contrast across the ACC and thus decreases the thermal current shear in the upper half of the water column. We observe that increasing the wind stress curl within the Southern Ocean in regions where the eastward velocities are higher than the Rossby wave speed is associated with isopycnals moving upward in the water column, effectively allowing dense Antarctic waters to penetrate a little further to the north, contributing to the reduction of density contrast in deep waters where it can have a large impact on transport. Our results support both the ideas that changes in large-scale overturning can affect the ACC (following Gnanadesikan and Hallberg 2000; Fučkar and Vallis 2007) and that changes in wind stress curl may also affect ACC transport [though not to the extent hypothesized by Warren et al. (1996)].

Although the range of ACC transports seen herein is significant, it is much smaller than the range seen in the CMIP5 models (Beadling et al. 2019) as well as in Russell et al. (2006). This suggests that though A_{Redi} coefficients differ greatly between models, they are unlikely to account for the majority of the differences in transport. Rather, it is likely that differences in overturning in the Northern Hemisphere, or large differences in the structure of Southern Ocean winds (processes which may be linked to each other) play the dominant role.

Our results also illustrate the impact of including more realistic representations of A_{Redi} in ocean models. The representation of A_{Redi} developed by Abernathey and Marshall (2013) produces a transport of 158 Sv, which is reasonable by the standards of CMIP3 or CMIP5, despite having A_{Redi} coefficients which exceed $10\,000\,\mathrm{m^2\,s^{-1}}$ in some locations. From this we conclude that these high values are occurring in locations where they have relatively weak impact on the density structure. The full 2D structure is important–zonally averaging the diffusion coefficient produces a much larger impact on transport. This may be because zonally averaging the diffusion coefficient raises it in places where Abernathey and Marshall (2013) find suppression of A_{Redi} by fast moving currents with larger tracer gradients. Future work will need to provide a fully three-dimensional picture of how this critical parameter varies, both in space and time.

Acknowledgments. This work was supported by the National Science Foundation under proposals FESD-1338814 and OCE-1766568 and by the Department of Energy under proposal DE-SC0019344. We thank Will Seviour, Jordan Thomas, Kyle Armour, Spencer Jones, and Peter Gent for comments on earlier versions of this manuscript and gratefully acknowledge computing resources provided by the Institute for Data Intensive Engineering and Science (IDIES) at Johns Hopkins University. Model climatologies are provided in NetCDF format at https://doi.org/10.7281/T1/IJO1FU.

REFERENCES

Abernathey, R. P., and J. Marshall, 2013: Global surface eddy diffusivities derived from satellite altimetry. *J. Geophys. Res. Oceans*, **118**, 901–916, https://doi.org/10.1002/jgrc.20066.

Alley, R. B., P. U. Clark, P. Huybrechts, and I. Joughin, 2005: Ice-sheet and sea-level changes. *Science*, **310**, 456–460, https://doi.org/10.1126/science.1114613.

——, S. Anandakrishnan, K. Christianson, H. J. Horan, A. Muto, B. R. Parizek, D. Pollard, and R. T. Walker, 2015: Oceanic forcing of ice-sheet retreat: West Antarctica and more. *Annu. Rev. Earth Planet. Sci.*, **43**, 207–231, https://doi.org/10.1146/annurev-earth-060614-105344.

Bahl, A. A., A. Gnanadesikan, and M. A. Pradal, 2019: Variations in ocean deoxygenation across earth system models: Isolating the role of parameterized lateral mixing. *Global Biogeochem. Cycles*, **33**, 703–724, https://doi.org/10.1029/2018GB006121.

Beadling, R. L., J. L. Russell, R. J. Stouffer, P. J. Goodman, and M. Mazloff, 2019: Assessing the quality of Southern Ocean circulation in CMIP5 AOGCM and earth system model simulations. *J. Climate*, **32**, 5915–5940, https://doi.org/10.1175/JCLI-D-19-0263.1.

Bentsen, M., and Coauthors, 2013: The Norwegian Earth System Model, NorESM1-M–Part 1: Description and basic evaluation of the physical climate. *Geosci. Model Dev.*, **6**, 687–720, https://doi.org/10.5194/gmd-6-687-2013.

Caldeira, K., and P. B. Duffy, 2000: The role of the Southern Ocean in uptake and storage of anthropogenic carbon dioxide. *Science*, **287**, 620–622, https://doi.org/10.1126/science.287.5453.620.

Cunningham, S. A., S. Alderson, B. King, and M. Brandon, 2003: Transport and variability of the Antarctic Circumpolar Current in Drake Passage. *J. Geophys. Res.*, **108**, 8084, https://doi.org/10.1029/2001JC001147.

Danabasoglu, G., and J. Marshall, 2007: Effects of vertical variations of thickness diffusivity in an ocean general circulation model. *Ocean Modell.*, **18**, 122–141, https://doi.org/10.1016/j.ocemod.2007.03.006.

Dee, D. P., and Coauthors, 2011: The ERA–Interim reanalysis: Configuration and performance of the data assimilation system. *Quart. J. Roy. Meteor. Soc.*, **137**, 553–597, https://doi.org/10.1002/qj.828.

Doddridge, E. W., J. Marshall, H. Song, J.-M. Campin, M. Kelley, and L. Nazarenko, 2019: Eddy compensation dampens Southern Ocean sea surface temperature response to westerly wind

trends. *Geophys. Res. Lett.*, **46**, 4365–4377, https://doi.org/10.1029/2019GL082758.

Donohue, K. A., K. L. Tracey, D. R. Watts, M. P. Chidichimo, and T. K. Chereskin, 2016: Mean Antarctic Circumpolar Current transport measured in Drake Passage. *Geophys. Res. Lett.*, **43**, 11 760–11 767, https://doi.org/10.1002/2016GL070319.

Dufour, C. O., J. L. Sommer, J. D. Zika, M. Gehlen, J. C. Orr, P. Mathiot, and B. Barnier, 2012: Standing and transient eddies in the response of the Southern Ocean meridional overturning to the southern annular mode. *J. Climate*, **25**, 6958–6974, https://doi.org/10.1175/JCLI-D-11-00309.1.

Dunne, J., and Coauthors, 2012: GFDL's ESM2 global coupled climate–carbon earth system models. Part I: Physical formulation and baseline simulation characteristics. *J. Climate*, **25**, 6646–6665, https://doi.org/10.1175/JCLI-D-11-00560.1.

Farneti, R., and P. R. Gent, 2011: The effects of the eddy-induced advection coefficient in a coarse-resolution coupled climate model. *Ocean Modell.*, **39**, 135–145, https://doi.org/10.1016/j.ocemod.2011.02.005.

Fogli, P., and Coauthors, 2009: INGV–CMCC carbon (ICC): A carbon cycle Earth system model. CMCC Tech. Rep. RP0061, 31 pp., http://www.cmcc.it/publications-meetings/publications/research-papers/rp0061-ingv-cmcc-carbon-icc-a-carbon-cycle-earth-system-model.

Frölicher, T. L., J. Sarmiento, D. Paynter, J. Dunne, J. Krasting, and M. Winton, 2015: Dominance of the Southern Ocean in anthropogenic carbon and heat uptake in CMIP5 models. *J. Climate*, **28**, 862–886, https://doi.org/10.1175/JCLI-D-14-00117.1.

Fučkar, N. S., and G. K. Vallis, 2007: Interhemispheric influence of surface buoyancy conditions on a circumpolar current. *Geophys. Res. Lett.*, **34**, L14605, https://doi.org/10.1029/2007GL030379.

Galbraith, E. D., and Coauthors, 2011: Climate variability and radiocarbon in the CM2Mc earth system model. *J. Climate*, **24**, 4230–4254, https://doi.org/10.1175/2011JCLI3919.1.

Gent, P. R., and J. C. McWilliams, 1990: Isopycnal mixing in ocean circulation models. *J. Phys. Oceanogr.*, **20**, 150–155, https://doi.org/10.1175/1520-0485(1990)020<0150:IMIOCM>2.0.CO;2.

——, and G. Danabasoglu, 2011: Response to increasing Southern Hemisphere winds in CCSM4. *J. Climate*, **24**, 4992–4998, https://doi.org/10.1175/JCLI-D-10-05011.1.

——, W. G. Large, and F. O. Bryan, 2001: What sets the mean transport through Drake Passage? *J. Geophys. Res.*, **106**, 2693–2712, https://doi.org/10.1029/2000JC900036.

Giglio, D., and G. C. Johnson, 2016: Subantarctic and polar fronts of the Antarctic Circumpolar Current and Southern Ocean heat and freshwater content variability: A view from Argo. *J. Phys. Oceanogr.*, **46**, 749–768, https://doi.org/10.1175/JPO-D-15-0131.1.

Gill, A. E., 1982: *Atmosphere–Ocean Dynamics*. Academic Press, 662 pp.

Gille, S. T., 1997: The Southern Ocean momentum balance: Evidence for topographic effects from numerical model output and altimeter data. *J. Phys. Oceanogr.*, **27**, 2219–2232, https://doi.org/10.1175/1520-0485(1997)027<2219:TSOMBE>2.0.CO;2.

Gnanadesikan, A., 1999: A simple predictive model for the structure of the oceanic pycnocline. *Science*, **283**, 2077–2079, https://doi.org/10.1126/science.283.5410.2077.

——, and R. W. Hallberg, 2000: On the relationship of the Circumpolar Current to Southern Hemisphere winds in coarse-resolution ocean models. *J. Phys. Oceanogr.*, **30**, 2013–2034, https://doi.org/10.1175/1520-0485(2000)030<2013:OTROTC>2.0.CO;2.

——, and Coauthors, 2006: GFDL's CM2 global coupled climate models. Part II: The baseline ocean simulation. *J. Climate*, **19**, 675–697, https://doi.org/10.1175/JCLI3630.1.

——, D. Bianchi, and M.-A. Pradal, 2013: Critical role for mesoscale eddy diffusion in supplying oxygen to hypoxic ocean waters. *Geophys. Res. Lett.*, **40**, 5194–5198, https://doi.org/10.1002/grl.50998.

——, M.-A. Pradal, and R. Abernathey, 2015a: Exploring the isopycnal mixing and helium heat paradoxes in a suite of earth system models. *Ocean Sci.*, **11**, 591–605, https://doi.org/10.5194/os-11-591-2015.

——, ——, and ——, 2015b: Isopycnal mixing by mesoscale eddies significantly impacts oceanic anthropogenic carbon uptake. *Geophys. Res. Lett.*, **42**, 4249–4255, https://doi.org/10.1002/2015GL064100.

Griffies, S. M., 1998: The Gent–McWilliams skew flux. *J. Phys. Oceanogr.*, **28**, 831–841, https://doi.org/10.1175/1520-0485(1998)028<0831:TGMSF>2.0.CO;2.

Hallberg, R., and A. Gnanadesikan, 2001: An exploration of the role of transient eddies in determining the transport of a zonally reentrant current. *J. Phys. Oceanogr.*, **31**, 3312–3330, https://doi.org/10.1175/1520-0485(2001)031<3312:AEOTRO>2.0.CO;2.

——, and ——, 2006: The role of eddies in determining the structure and response of the wind-driven Southern Hemisphere overturning: Results from the Modeling Eddies in the Southern Ocean (MESO) project. *J. Phys. Oceanogr.*, **36**, 2232–2252, https://doi.org/10.1175/JPO2980.1.

Hughes, C. W., 2005: Nonlinear vorticity balance of the Antarctic Circumpolar Current. *J. Geophys. Res.*, **110**, C11008, https://doi.org/10.1029/2004JC002753.

Ito, T., M. Woloszyn, and M. Mazloff, 2010: Anthropogenic carbon dioxide transport in the Southern Ocean driven by Ekman flow. *Nature*, **463**, 80–83, https://doi.org/10.1038/nature08687.

Johns, T. C., and Coauthors, 2006: The new Hadley Centre climate model (HadGEM1): Evaluation of coupled simulations. *J. Climate*, **19**, 1327–1353, https://doi.org/10.1175/JCLI3712.1.

Johnson, G. C., and H. L. Bryden, 1989: On the size of the antarctic circumpolar current. *Deep-Sea Res.*, **36A**, 39–53, https://doi.org/10.1016/0198-0149(89)90017-4.

Jones, D. C., T. Ito, and N. S. Lovenduski, 2011: The transient response of the Southern Ocean pycnocline to changing atmospheric winds. *Geophys. Res. Lett.*, **38**, L15604, https://doi.org/10.1029/2011GL048145.

Karsten, R. H., and J. Marshall, 2002: Testing theories of the vertical stratification of the ACC against observations. *Dyn. Atmos. Oceans*, **36**, 233–246, https://doi.org/10.1016/S0377-0265(02)00031-3.

Kistler, R., and Coauthors, 2001: The NCEP–NCAR 50-Year Reanalysis: Monthly means CD-ROM and documentation. *Bull. Amer. Meteor. Soc.*, **82**, 247–268, https://doi.org/10.1175/1520-0477(2001)082<0247:TNNYRM>2.3.CO;2.

Langlais, C. E., S. R. Rintoul, and J. D. Zika, 2015: Sensitivity of Antarctic Circumpolar Current transport and eddy activity to wind patterns in the southern ocean. *J. Phys. Oceanogr.*, **45**, 1051–1067, https://doi.org/10.1175/JPO-D-14-0053.1.

Ledwell, J. R., A. J. Watson, and C. S. Law, 1998: Mixing of a tracer in the pycnocline. *J. Geophys. Res.*, **103**, 21 499–21 529, https://doi.org/10.1029/98JC01738.

Lumpkin, R., and P. Flament, 2001: Lagrangian statistics in the central North Pacific. *J. Mar. Syst.*, **29**, 141–155, https://doi.org/10.1016/S0924-7963(01)00014-8.

Marshall, G. J., 2003: Trends in the Southern Annular Mode from observations and reanalyses. *J. Climate*, **16**, 4134–4143, https://doi.org/10.1175/1520-0442(2003)016<4134:TITSAM>2.0.CO;2.

Meijers, A. J. S., 2014: The Southern Ocean in the coupled model intercomparison project phase 5. *Philos. Trans. Roy. Soc.*, **372A**, 20130296, https://doi.org/10.1098/RSTA.2013.0296.

——, E. Shuckburgh, N. Bruneau, J.-B. Sallee, T. J. Bracegirdle, and Z. Wang, 2012: Representation of the Antarctic circumpolar current in the CMIP5 climate models and future changes under warming scenarios. *J. Geophys. Res.*, **117**, C12008, https://doi.org/10.1029/2012JC008412.

Meredith, M. P., and A. M. Hogg, 2006: Circumpolar response of Southern Ocean eddy activity to a change in the southern annular mode. *Geophys. Res. Lett.*, **33**, L16608, https://doi.org/10.1029/2006GL026499.

Morrison, A. K., and A. McC. Hogg, 2013: On the relationship between southern ocean overturning and ACC transport. *J. Phys. Oceanogr.*, **43**, 140–148, https://doi.org/10.1175/JPO-D-12-057.1.

Munday, D. R., H. L. Johnson, and D. P. Marshall, 2013: Eddy saturation of equilibrated circumpolar currents. *J. Phys. Oceanogr.*, **43**, 507–532, https://doi.org/10.1175/JPO-D-12-095.1.

Munk, W. H., and E. Palmén, 1951: Note on the dynamics of the antarctic circumpolar current. *Tellus*, **3**, 53–55, https://doi.org/10.3402/tellusa.v3i1.8609.

Naveira Garabato, A. C., K. L. Polzin, R. Ferrari, J. D. Zika, and A. Forryan, 2016: A microscale view of mixing and overturning across the antarctic circumpolar current. *J. Phys. Oceanogr.*, **46**, 233–254, https://doi.org/10.1175/JPO-D-15-0025.1.

Pradal, M.-A., and A. Gnanadesikan, 2014: How does the Redi parameter for mesoscale mixing impact global climate in an earth system model? *J. Adv. Model. Earth Syst.*, **6**, 586–601, https://doi.org/10.1002/2013MS000273.

Pritchard, H., S. Ligtenberg, H. Fricker, D. Vaughan, M. Van den Broeke, and L. Padman, 2012: Antarctic ice-sheet loss driven by basal melting of ice shelves. *Nature*, **484**, 502–505, https://doi.org/10.1038/nature10968.

Redi, M. H., 1982: Oceanic isopycnal mixing by coordinate rotation. *J. Phys. Oceanogr.*, **12**, 1154–1158, https://doi.org/10.1175/1520-0485(1982)012<1154:OIMBCR>2.0.CO;2.

Rintoul, S., 2009: Antarctic circumpolar current. *Encyclopedia of the Ocean Sciences*, 2nd ed. Academic Press, 178–190.

Russell, J. L., R. J. Stouffer, and K. W. Dixon, 2006: Intercomparison of the Southern Ocean circulations in IPCC coupled model control simulations. *J. Climate*, **19**, 4560–4575, https://doi.org/10.1175/JCLI3869.1.

Seviour, W. J. M., A. Gnanadesikan, D. Waugh, and M.-A. Pradal, 2017: Transient response of the Southern Ocean to changing ozone: Regional responses and physical mechanisms. *J. Climate*, **30**, 2463–2480, https://doi.org/10.1175/JCLI-D-16-0474.1.

Starr, V. P., 1948: An essay on the general circulation of the Earth's atmosphere. *J. Meteor.*, **5**, 39–43, https://doi.org/10.1175/1520-0469(1948)005<0039:AEOTGC>2.0.CO;2.

Straub, D. N., 1993: On the transport and angular momentum balance of channel models of the Antarctic Circumpolar Current. *J. Phys. Oceanogr.*, **23**, 776–782, https://doi.org/10.1175/1520-0485(1993)023<0776:OTTAAM>2.0.CO;2.

Tansley, C. E., and D. P. Marshall, 2001: On the dynamics of wind-driven circumpolar currents. *J. Phys. Oceanogr.*, **31**, 3258–3273, https://doi.org/10.1175/1520-0485(2001)031<3258:OTDOWD>2.0.CO;2.

Wang, L., 1994: A linear homogeneous model for topographic control of the Antarctic Circumpolar Current. *J. Mar. Res.*, **52**, 649–685, https://doi.org/10.1357/0022240943076993.

Warren, B. A., J. H. Lacasce, and P. E. Robbins, 1996: On the obscurantist physics of "form drag" in theorizing about the circumpolar current. *J. Phys. Oceanogr.*, **26**, 2297–2301, https://doi.org/10.1175/1520-0485(1996)026<2297:OTOPOD>2.0.CO;2.

Whitworth, T., and R. G. Peterson, 1985: Volume transport of the antarctic circumpolar current from bottom pressure measurements. *J. Phys. Oceanogr.*, **15**, 810–816, https://doi.org/10.1175/1520-0485(1985)015<0810:VTOTAC>2.0.CO;2.

Worthington, L., 1981: The water masses of the world ocean: Some results of a fine-scale census. *Evolution of Physical Oceanography, Scientific Surveys in Honor of Henry Stommel*, B. A. Warren and C. Wunsch, Eds., MIT Press, 42–60.